Semiconductor Science and Technology

PAPER • **OPEN ACCESS**

Design of step-graded AlGaN buffers for GaN-on-Si heterostructures grown by MOCVD

To cite this article: Saptarsi Ghosh *et al* 2023 *Semicond. Sci. Technol.* **38** 044001

OPEN ACCESS
IOP Publishing
Semiconductor Science and Technology
Semicond. Sci. Technol. **38** (2023) 044001 (16pp)
https://doi.org/10.1088/1361-6641/acb9b6

Design of step-graded AlGaN buffers for GaN-on-Si heterostructures grown by MOCVD

Saptarsi Ghosh[1], Alexander M Hinz[2], Martin Frentrup[1], Saiful Alam[3], David J Wallis[1,3] and Rachel A Oliver[1,*]

[1] Department of Materials Science and Metallurgy, University of Cambridge, 27 Charles Babbage Rd, Cambridge CB3 0FS, United Kingdom
[2] Fraunhofer FEP, Winterbergstraße 28, 01277 Dresden, Germany
[3] Centre for High Frequency Engineering, University of Cardiff, 5 The Parade, Newport Road, Cardiff CF24 3AA, United Kingdom

E-mail: rao28@cam.ac.uk

Received 28 October 2022, revised 4 February 2023
Accepted for publication 7 February 2023
Published 22 February 2023

Abstract

For the growth of low-defect crack-free GaN heterostructures on large-area silicon substrates, compositional grading of AlGaN is a widely adapted buffer technique to restrict the propagation of lattice-mismatch induced defects and balance the thermal expansion mismatch-induced tensile stress. So far, a consolidation of the design strategy of such step-graded buffers has been impaired by the incomplete understanding of the effect of individual buffer design parameters on the mechanical and microstructural properties of the epilayers. Herein, we have analyzed a series of metal-organic chemical vapor deposition grown GaN/graded-AlGaN/AlN/Si heterostructures through *in situ* curvature measurements and post-growth x-ray diffraction (XRD). Our results reveal that in such epi structures, the GaN layer itself induces more compressive stress than the AlGaN buffer, but the underlying AlGaN layers dictate the magnitude of this stress. Furthermore, for a fixed AlGaN buffer thickness, the mean-stress accumulated during the GaN growth is found to be correlated with its structural properties. Specifically, one μm thick GaN layers that acquire 1.50 GPa or higher compressive mean-stress are seen to possess $20\bar{2}1$ XRD ω-FWHM values less than 650 arc-sec. Also, the evolution of instantaneous stresses during the growth of the AlGaN layers is found to be a valuable indicator for buffer optimization, and composition difference between successive layers is established as a crucial criterion. The results also show that increasing the total buffer thickness (for a fixed number of steps) or increasing the number of steps (for a fixed total buffer thickness) may not always be beneficial. Irrespective of the buffer thickness, optimized high electron mobility transistor structures show similarly low sheet-resistance ($\sim$350 Ω $\square$)$^{-1}$ and high mobility ($\sim$2000 cm^2 V^{-1} s^{-1}) at room temperature.

* Author to whom any correspondence should be addressed.

Supplementary material for this article is available online

Keywords: GaN-on-Si, AlGaN buffer, MOCVD, heteroepitaxy

(Some figures may appear in colour only in the online journal)

1. Introduction

Due to the immaturity of bulk nitride substrates, heteroepitaxial growth of wide bandgap nitride thin-film devices on large-area silicon substrates has been a promising route for enabling their scalable and cost-effective commercialization [1–3]. To date, two major obstacles stemming from the large lattice (∼17%) and thermal expansion (∼54%) mismatch between Si (111) and wurtzite GaN (and its alloys with Al and In) have proven to be a limitation on such integration. The former results in numerous dislocations in the epilayers, whereas the different coefficients of thermal expansion (CTE) lead to large tensile stresses during cooling from typical growth temperatures ($\geqslant$1000 °C), often culminating in cracking. To tackle these challenges, buffer layers play a crucial role in defect-reduction and stress-management for GaN-on-Si devices. Firstly, they partially annihilate threading dislocations (TDs) generated at the Si substrate/AlN nucleation layer (NL) interface from propagating into the functional layers [4–7]. Furthermore, they also induce compressive in-plane stress during the growth process to compensate for the post-deposition thermal tensile stress. As attempts to grow GaN directly on high-temperature (HT) AlN results in heavily cracked epilayers [8, 9], three buffer design strategies have been extensively explored in the last two decades. Among these, graded AlGaN buffers avoid the time-consuming periodic ramping of temperature, pressure, and precursor flows needed for low-temperature (LT) AlN interlayers or AlN/GaN superlattice buffers. In such AlGaN multilayers, the gradation involves changing the AlN mole fraction from a higher starting Al-composition ($Al_zGa_{1-z}N$) near the AlN NL to a lower value ($Al_xGa_{1-x}N$, $x < z$) near the GaN. This is done in successive steps in a step-graded buffer and in a continuous manner in a smoothly-graded buffer. In both, this sequential decrease in the Al-composition (and the increase in lattice constant) is intended to cause the AlGaN and GaN layers to grow under compression during epitaxy. The principle aim is to achieve a net strain after cooldown which is either compressive or, if tensile, limits the strain energy in GaN below the threshold required for crack propagation. In this article, we focus on buffers with step-gradation and as long as there is a relatively low mismatch between subsequent layers, these avoid the generation of new dislocations at the interface between successive AlGaN steps that have been reported [10] with the other two strategies involving GaN/AlN interfaces. Mechanistic properties of such step-graded AlGaN buffers in GaN-based heterostructures continues [11–13] to be a topic of great interest. In addition to the existing devices, the emergence of transistors [14] and UV emitters [15] with high Al-composition layers, devices utilizing the electronic and photonic functionality [16] of the AlGaN grading itself, and substrate-removed heterogeneously-integrated [17, 18] devices have further strengthened the need for a deeper understanding of the tuning parameters of these buffers.

In particular, what has hindered the development of a generic step-graded design guideline is the simultaneous availability of several variables. These include compositions of the grade, total thickness, number of layers, and thickness ratio (i.e. the thickness of the individual layers for a fixed total thickness) for which the individual and correlated effects are still not clearly established. For instance, in their thickness optimization study, Cheng and co-workers [9] found that only the 750 nm thick step-graded AlGaN buffer yielded a compressive mean-stress whereas both thicker and thinner buffers resulted in the mean-stress becoming tensile. Separately, in their investigation, Xu *et al* [19] found the optimized AlGaN buffer thickness to be 300 nm as both thicker and thinner buffers produced heavily-cracked 2 μm thick GaN epilayers. These results clearly suggest the involvement of competing strain mechanisms with changes in buffer thickness. Confusion also remains on what is the optimum number of steps in a buffer. Examples of step-graded buffers including from two to seven distinct layers can be found in the literature [7, 9, 20–26] though crack-free GaN on Si using a single AlGaN layer [27–29] as the buffer has also been reported. The other parameters i.e. the choice of the individual compositions and the thickness ratio of the different layers also differ widely among groups. However, systematic investigations focusing on the influence of these two parameters on the effectiveness of the buffer are even scarcer. Altogether, as a result of the uncertainties involved, reports can be found where even the best-optimized structure is not completely crack-free [24] or does not satisfy the limits of processing compliance [23]. Hence, instead of solely relying on the AlGaN buffer to ensure stress-management, the practice of supplementing these with AlN interlayers [30, 31] or AlN/GaN superlattices [32] in the same buffer structure is also common.

As this lack of understanding cannot be addressed by studies [4, 33] comparing different buffer design technologies, the present work scrutinizes GaN-on-Si heterostructures with closely related step-graded AlGaN buffers to show how stress-evolution and microstructure are influenced by individual design parameters. Considering that absolute results are often not transferrable from one metal-organic chemical vapor deposition (MOCVD) reactor to another, the primary motivation of this article is to provide a generic framework that can guide step-graded buffer design process for improved control of stress and defects, even under the constraints of certain

parameters being fixed. Alongside the investigations on buffers employing LT-AlN layers [34, 35] and AlN/GaN superlattices [6, 36], establishing the 'control knobs' for graded AlGaN buffers should open up more options for nitrides-on-Si manufacturing, enabling further proliferation of the technology.

2. Experimental Details

The studied structures were grown in a vertical-flow high-speed rotating-disc (∼1000 rpm.) single wafer MOCVD reactor (Veeco Propel™) with trimethylgallium (TMGa), trimethylaluminum (TMAl), and ammonia (NH_3) as the precursors and hydrogen (H_2) as the carrier gas. P-type Si (111) substrates,1 mm thick and 150 mm in diameter, were first heated in H_2 ambient at 1100 °C to remove the native surface oxide *in-situ* without any external chemical pre-treatment. This was followed by the growth of a two-temperature AlN NL to prevent the melt-back etching [37, 38] associated with Ga-Si eutectic formation [39, 40]. The subsequent epi-growth consisted of the deposition of different step-graded AlGaN buffers and finally a 1 μm thick GaN layer, as illustrated in the schematic in figure 1 (left) for a heterostructure with 3-step AlGaN buffer. Two different AlGaN buffer thicknesses (∼1 μm for wafers A13 to D15 and ∼1.7 μm for wafers A25 to D23) were grown for this analysis. Both symmetric (i.e. the thickness of each AlGaN layer being equal) and asymmetric designs were studied. The composition difference between the end layers was approximately equally distributed among the intermediate layers and the eight structures were designed to have at least one closely related variant where only one design parameter was changed. The latter allowed the pinpointing of the influence of individual parameters. Note that the first numerical in each wafer name indicates the rounded up total thickness in μm and the second numerical denotes the number of steps. The variations in the composition and individual thickness of the AlGaN layers are detailed in table 1.

The AlN layers were grown in two steps. The first 10 nm were grown at a temperature of 750 °C and the rest of the NL at 1070 °C. The temperatures during the growth of the AlGaN buffers, and the GaN layers were 1035 °C, and 1050 °C, respectively. The group V/III molar ratio during the $Al_xGa_{1-x}N$ layer growths was 300 for compositions with low AlN mole fractions ($0.25 \leqslant x \leqslant 0.50$) and 150 for high AlN mole fractions ($0.50 < x \leqslant 0.83$). Such flow conditions were found to minimize the parasitic gas-phase reactions between TMAl and NH_3 and improve the incorporation efficiency of TMAl. For the GaN growth, the V/III ratio was increased to 1500. The secondary electron image of an as-grown heterostructure with a 3-step AlGaN buffer is shown in figure 1(right). Individual layers are distinguishable in the image with an increase in their brightness with a decrease in the Al-content. Note that, near the final interface between $Al_{0.33}Ga_{0.67}N$ and GaN, a gradual change in brightness in the GaN layer is also observed. This, however, likely stems from either a gradual change in the strain-induced piezoelectric field within the layer or the accumulation of holes at the interface due to the valance band offset and polarization discontinuity, both of which can influence the secondary electron emission.

During growth, *in situ* process monitoring tools (RT-200™ and DRT-210™) continuously measured the curvature, temperature, and reflectivity of the wafer. Interferometry-based intensity variation of a 650 nm laser reflected from the wafer gave the thickness of the epilayers in real-time. Simultaneously, the spatial displacement of the same laser beam on a quadrant detector provided the curvature assuming a spherical bow.

By the formulae detailed in the following section, changes of curvature during growth were used to calculate the change of stress-thickness with thickness to quantify the growth-induced stresses. As an example, the real-time evolution of wafer curvature during the growth of wafer A13 is shown in figure 2(a). It can be seen that before the start of the AlN growth at 1070 °C, the wafer was already concavely bowed due to the temperature difference between the front and back of the wafer which were in contact with the gas-phase boundary layer and the susceptor, respectively [1]. This initial wafer bowing is a reversible effect whose influence is fully removed once the temperature difference vanishes after cool-down to room temperature. During deposition of the AlN layer, the curvature became more positive i.e. the wafer became more concave. As the AlN growth takes place at a constant temperature, this change of curvature is due to the stress originating from the growth of the layer, and the sign of the change indicates that the involved growth stress was tensile. Before the growth of the next layer, the first AlGaN layer, the growth temperature was reduced by 25 °C. This led to a minute decrease in wafer curvature indicated by the red circles in figure 2(a). This is the cumulative effect of a reduced temperature gradient between the front and the back of the wafer as well as the different expansion of the AlN and Si caused by the change in temperature. While the earlier of these two sources is fully reversible the later one will add to the final bow of the wafer in the form of thermal tensile stress. However, in terms of the stress-thickness analysis, which is the primary focus of this work, these temperature changes have no influence as no change in layer thickness takes place during these periods of no growth. Further analysis of the data in figure 2(a) for individual layers shows that in contrast to the AlN, growth of the subsequent AlGaN buffer and GaN layer increased the curvature in the negative direction indicating compressive growth-stresses, and the wafer eventually became convex at the growth temperature. The curvature at the end of the GaN growth was sufficiently convex to offset the tensile thermal stress induced during cooldown, and hence, the curvature at room temperature was also convex for all the wafers (see figure S1 in the supplementary material). Note that the periodic discontinuities in both datasets arise from the extinction of the laser signal at the trough of each reflectivity oscillation, causing sharp peaks in curvature [5, 41] and these regions were excluded from analysis. It is worth mentioning that AlGaN layers are susceptible to 3D roughening and buried pit formation [23, 42]. However, as shown in figure 2(b), the nearly constant amplitude and average intensity of the reflectivity oscillations throughout the growth confirm that the

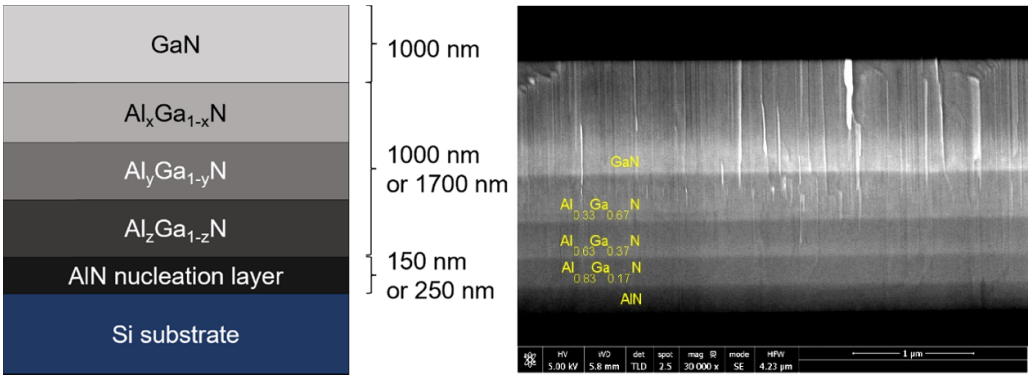

Figure 1. (Left) Schematic of a representative GaN-on-Si heterostructure with 3-step AlGaN buffer that has successively deceasing Al composition ($x < y < z$). The 5-step buffers had two additional AlGaN layers between the AlN and GaN. (Right) Secondary electron image of the heterostructure B13 with discernible contrast between the successive AlN, AlGaN, and GaN layers. The scalebar in the image is one μm.

Table 1. Details of the MOCVD grown GaN/graded-AlGaN/AlN on Si heterostructures. The difference between each structure and its closest variant is identified. All the listed mean stress (with negative sign denoting compressive stress) and wafer bow are derived from *in situ* curvature values at room temperature.

Wafer ID	AlN NL	Nominal thickness and composition of the buffer layers (every wafer includes a $\sim$1.0 μm thick GaN layer on top of the buffer)	Modification	Mean-stress of entire epi	Wafer bow
		Samples with $\sim$1.0 μm thick AlGaN buffer			
A13	150 nm	250 nm $Al_{0.83}Ga_{0.17}N$/ 300 nm $Al_{0.63}Ga_{0.37}N$/ 400 nm $Al_{0.33}Ga_{0.67}N$	AlN thinner than B13	-0.16 GPa	30 μm, convex
B13	250 nm	250 nm $Al_{0.83}Ga_{0.17}N$/ 300 nm $Al_{0.63}Ga_{0.37}N$/ 400 nm $Al_{0.33}Ga_{0.67}N$	—	-0.22 GPa	42 μm, convex
C13	250 nm	250 nm $Al_{0.78}Ga_{0.22}N$/ 350 nm $Al_{0.50}Ga_{0.50}N$/ 450 nm $Al_{0.25}Ga_{0.75}N$	Compositions different than B13	-0.23 GPa	44 μm, convex
D15	250 nm	200 nm $Al_{0.78}Ga_{0.22}N$/ 200 nm $Al_{0.65}Ga_{0.35}N$/ 200 nm $Al_{0.50}Ga_{0.50}N$/200 nm $Al_{0.36}Ga_{0.64}N$/ 200 nm $Al_{0.25}Ga_{0.75}N$	Two more steps than C13, different thicknesses	-0.28 GPa	54 μm, convex
		Samples with $\sim$1.7 μm thick AlGaN buffer			
A25	250 nm	350 nm $Al_{0.78}Ga_{0.22}N$/ 350 nm $Al_{0.65}Ga_{0.35}N$/ 350 nm $Al_{0.50}Ga_{0.50}N$/350 nm $Al_{0.36}Ga_{0.64}N$/ 350 nm $Al_{0.25}Ga_{0.75}N$	Layer thicknesses of D15 equally increased	-0.14 GPa	34 μm, convex
B25	250 nm	200 nm $Al_{0.78}Ga_{0.22}N$/ 200 nm $Al_{0.65}Ga_{0.35}N$/ 350 nm $Al_{0.50}Ga_{0.50}N$/500 nm $Al_{0.36}Ga_{0.64}N$/ 500 nm $Al_{0.25}Ga_{0.75}N$	Bottom (top) two layers thinner (thicker) than A25	-0.12 GPa	31 μm, convex
C25	250 nm	500 nm $Al_{0.78}Ga_{0.22}N$/ 500 nm $Al_{0.65}Ga_{0.35}N$/ 350 nm $Al_{0.50}Ga_{0.50}N$/200 nm $Al_{0.36}Ga_{0.64}N$/ 200 nm $Al_{0.25}Ga_{0.75}N$	Top (bottom) two layers thicker (thinner) than A25	-0.12 GPa	31 μm, convex
D23	250 nm	420 nm $Al_{0.83}Ga_{0.17}N$/ 550 nm $Al_{0.63}Ga_{0.37}N$/ 720 nm $Al_{0.33}Ga_{0.67}N$	Layer thicknesses of B13 equally increased	-0.11 GPa	27 μm, convex

process conditions ensured smooth 2D layer growth. A similar trend of *in situ* curvature and reflectivity variation during growth was observed for all the wafers.

After growth, the wafers were inspected in an Olympus Nomarski optical microscope and in a Bruker Dimension Icon atomic force microscope (AFM) operated in Peakforce™ tapping mode to examine the surface topography across different length scales (see figures S2 and S3 in the supplementary material). The compositions of the individual AlGaN buffer layers were ascertained from $20\bar{2}5$ reciprocal space maps acquired in a PANlytical Empyrean high-resolution x-ray Diffractometer (HRXRD) equipped with a two-bounce hybrid monochromator at the source and a 3D PIXcel™ detector operated in frame-based mode (see figure S4 in the supplementary material). For the assessment of the structural quality, rocking curves of GaN reflections (with reduced beam widths to supress any possible broadening effects by wafer bow) were acquired in double-axis geometry (with a divergence slit but without any analyzer crystal). This diffractometer (a Philips X'Pert HRXRD) was equipped with an asymmetric

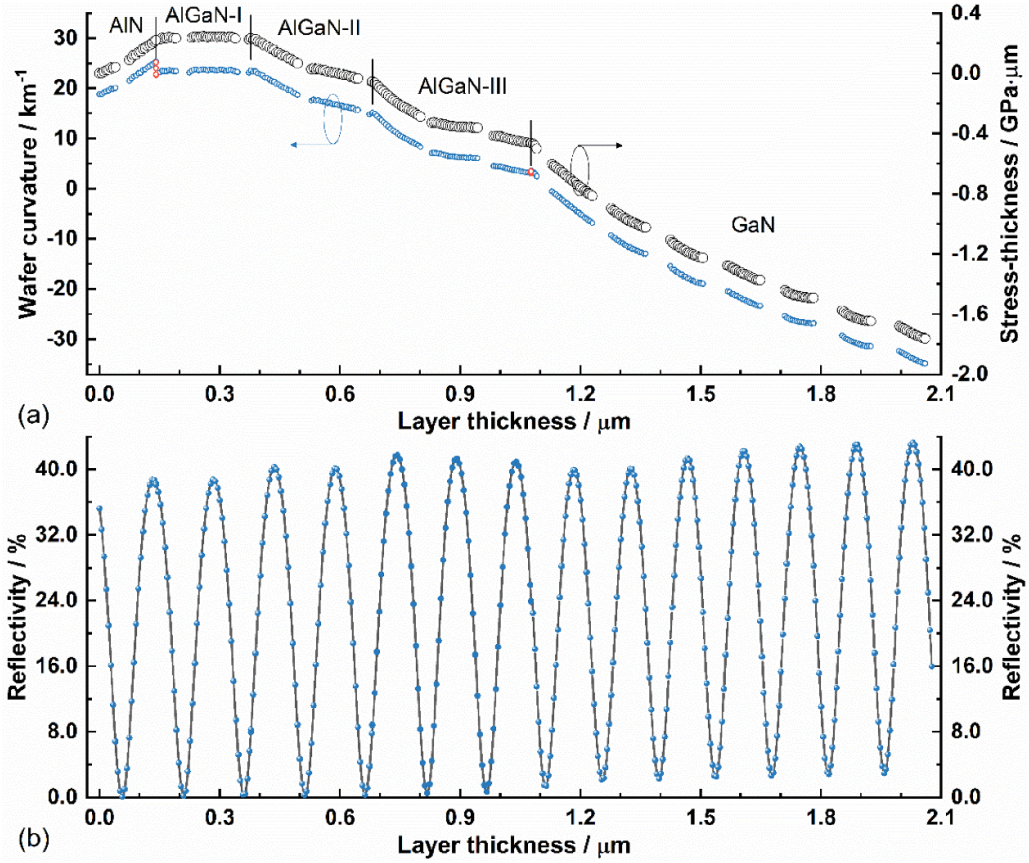

Figure 2. (a) Real-time evolution of curvature (small circles, blue) with thickness during the growth of the epilayers of wafer A13. Also shown is the as-calculated stress-thickness (large circles, black) versus thickness profile which imitates the curvature data. The beginning of the AlN growth (i.e. zero layer thickness) marks the zero of the stress-thickness curves. The changes in curvature (marked as red circles) during transition from AlN to AlGaN and AlGaN to GaN growth conditions are due to the changes in growth temperature and do not influence stress-thickness data. In these images, for visual clarity, only one representative experimental data point is shown for approximately every 3 nm. (b) The reflectivity oscillations which are simultaneously acquired with curvature during the layer growth.

four-bounce Ge 220 monochromator and 5 × 5 mm^2 cross-slits at source as well as a proportional-counter on the detector site. ω-Rocking curves for both symmetric 0002 and skew-symmetric 20$\bar{2}$1 reflections were acquired for these measurements, and their peak widths (FWHM, full-width at half maximum) were analyzed as a measure of reflection broadening by defects. The efficacy of each buffer was judged from two aspects of the GaN layer on top, namely the mean compressive stress accumulated during the GaN layer growth and the structural quality of the GaN layer as a measure of its defect density. For Hall-effect measurements, 1 × 1 cm^2 square samples with lithographically processed Ti/Al/Ti/Au ohmic contacts were characterized in an Ecopia hall-effect measurement system (HMS) equipped with 0.5 T magnets.

3. Theoretical Framework

The stress analysis is based on a formalism [43–45] that considers the equilibrium of forces and moments which induce a change in the curvature of a flat bulk substrate upon the deposition of a strained thin layer. For an in-plane stress whose magnitude can vary within the layer along the out-of-plane growth direction (z), the corresponding force-per-width is given by

$$\overline{F} = <\sigma> h_f = \int_0^{h_f} \sigma(h)\, dh \tag{1}$$

where $\sigma(h)$ is the in-plane stress at the thickness h and width is the layer dimension in the direction orthogonal to both the force vector and z. Here $<\sigma>$ represents the thickness-averaged stress or mean-stress of the entire layer having thickness h_f. When h_f is small compared to the substrate thickness, this force-per-width or stress-thickness product (expressed in N/m or in GPa μm) is directly related to the induced curvature change $\Delta\kappa$ of the film-substrate ensemble by the modified Stoney's equation

$$<\sigma> h_f = \frac{E_s h_s^2 \Delta\kappa}{6(1-\gamma_s)} \tag{2}$$

where E_s, h_s, and γ_s are the Young's modulus, thickness, and Poisson's ratio of the elastically isotropic substrate material (silicon (111) with respective values of 160 GPa, 1000 μm, and 0.22 [46, 47]). As per convention, positive stress (i.e.

tensile) induces a positive increase of the wafer curvature. Note that the first order terms involving the thickness ratio are ignored [48, 49] in equation (1) owing to its small value for the present structures (<0.003) and due to the bulk modulus of the epilayer and the substrate material being of the same order.

For a multilayer film, equation (2) can be further extended when the total curvature is a non-weighted superposition of the contributions from each layer i.e. $\Delta\kappa = \sum_{i=0}^{n} \Delta\kappa_i$. This approximation enables us to deduce the mean-stress of a multilayer film from the post-growth curvature. Thus, this mean-stress is effectively related to the wafer-bow ($\propto \kappa^{-1}$) for a substrate that was flat before growth of the thin film.

For quantification of the instantaneous stress, the time derivative of equation (1) needs to be considered instead

$$\frac{d\bar{F}}{dt} = \sigma_{\mathrm{ins}}(h)\frac{dh}{dt} + \int_0^{\mathrm{h}} \frac{\partial\sigma(h,t)}{\partial t}\,dh \tag{3}$$

wherein the first term on the right-hand side denotes the instantaneous stress, $\sigma_{\mathrm{ins}}(h)$,with which the incremental layer dh is grown in time dt. The second term could be any time-dependent change in stress in the layers (with total thickness h) on top of which this incremental layer is deposited. The net contribution of these two terms is thus proportional to the rate of change of curvature, i.e. $\frac{E_s h_s^2}{6(1-\gamma_s)}\frac{d}{dt}$ from (1)–(3). In the absence of time-dependent stress-relaxation of the underlying layer, the second term of-course vanishes and the rate of change of curvature directly yields $_{\mathrm{ins}}(h)$. Thus, a continuous measurement of the curvature while the film is being deposited at a known growth rate can be used to quantify the stresses in real-time. In such stress measurements, the resolution in principle is limited only by the sensitivity of the curvature system. Crack generation during the growth itself can act as a source of stress-relaxation characterized by an abrupt change in curvature, but no evidence of such was experienced during any of the growth experiments listed in this study. Also, depending on the material system and deposition conditions, film stresses can change owing to processes occurring in the bulk. This can be confirmed by observing the stress evolution during growth interruptions [44]. Hence, periods of ∼10 min long interrupts were intentionally inserted during some of the growth runs, but the curvature remained unchanged during these growth interrupts. This confirmed that except growth-induced stress at the growth front no other stress-generation/relaxation mechanisms were involved at the growth temperature. Thus, the second term in equation (2) becomes zero for the investigated structures, and all the instantaneous slope changes in the stress-thickness versus thickness curves at a fixed temperature are attributed to the deposition of the incremental layer.

For this study, the stress-thickness versus thickness data was first calculated from the real-time changes in the wafer curvature during epi-growth [50]. Then, the as-calculated stress-thickness profile of each buffer layer was fitted with piecewise linear functions for which the number of intervals (two or three, depending upon the layer thickness) were decided by the algorithm (Origin™ version 2020) for best least-square fits. The slopes for the first and last segments of each AlGaN layer were considered as the initial and final instantaneous stress for the buffer layers. Note that for the $Al_{0.83}Ga_{0.17}N$ layers of the 1 μm buffers and for all the AlN NLs, attempts to fit the experimental data in a similar manner resulted in 'overfitting' i.e. the model had more parameters (segments in this case) than can be justified by data. Hence, these layers were fitted with straight lines (i.e. with fixed slope). Based on the data from all wafers, on average, (560 ± 147) and (755 ± 57) number of data points were fitted per 100 nm for the AlGaN layers and the AlN NLs, respectively. The maximum fitting error for the slopes was ±0.02 GPa and usually an order less. However, the same layer in different structures (i.e. grown on the same underlying template) yielded a difference in slope of ±0.1 GPa and this run-to-run variation is considered as the uncertainty in calculated instantaneous stress.

Apart from the mean-stress for the entire epi-stacks and instantaneous-stress for incremental thicknesses, a third stress related metric was also considered for the present analysis, namely the mean-stress ($\overline{\sigma_i}$) generated during the growth of the i-th layer. It is defined as

$$\overline{\sigma_i} h_i = \int_0^{\mathrm{h_i}} \sigma(h)\,dh = \frac{E_s h_s^2 \Delta\kappa_i}{6(1-\gamma_s)} \tag{4}$$

where h_i is the thickness of the i-th layer which induces a total curvature change of $\Delta\kappa_i$ during the growth of the layer. Extraction of $\overline{\sigma_i}$ of a layer does not involve any fitting since only the initial and final values of stress-thickness during a layer growth are relevant. The uncertainty in the calculated mean-stress was considered to be due to the variation of thickness across the wafers measured from reflectivity traces measured at the center and outer edge of each wafer. This thickness variation was largest for the GaN layers (∼3%) which were also the thickest, resulting in a maximum uncertainty of 0.05 GPa for GaN. Though for AlN and AlGaN layers the variations were lower, a similar 3% difference is considered as uncertainty for these layers and the resulting absolute uncertainties in the mean-stress are considered as error bars for each layer. The variation in the extracted mean-stress derived from repeated growth runs were lower. Note that $\overline{\sigma_i}$ can be considered as the growth-temperature equivalent to room-temperature stress values usually deduced from Raman measured peak-shifts or XRD measured lattice-constants which also probe and average across the entire layer.

4. Results

4.1. Stresses in epitaxial heterostructures

For the present analysis, three stress terms were quantified namely real-time instantaneous-stress ($_{ins}$), mean-stress of each layer ($\overline{\sigma_i}$), and mean-stress of the entire heterostructure ($\bar{\sigma}$). These relate to incremental change of curvature, change of curvature due to each layer, and change of curvature due to the entire epi-stack of the wafer, respectively. Note that the

former two are calculated at the growth temperature whereas the latter is calculated at room temperature i.e. after cool-down. Among these, $\bar{\sigma}$ and wafer-bow at room temperature for each wafer is listed in table 1 and these include contribution from both growth-induced stresses and thermal expansion coefficient mismatch related stresses. The $\leqslant 50$ μm bow of the wafers ensure their eligibility for full-wafer lithography in automated tools and validate the technological relevance of the study. The fact that similarly low and compressive $\bar{\sigma}$ were achieved for different compositions and thicknesses of the buffer layers is in contrast with previous reports that suggested only a narrow thickness window exists for realizing compressively stressed GaN-on-Si with step-graded buffers. Nonetheless, to gain insight about the involved mechanisms, we need to focus on $_{ins}$ and $\overline{\sigma_i}$ derived from the real-time evolution of stress-thickness (i.e. product of stress and thickness, in GPa μm) during growth.

4.2. AlN nucleation layer

The curves for the 1.0 μm buffers are plotted in figure 3. In all the studied structures, the AlN NL showed a constant positive increase of stress-thickness during growth, confirming tensile stress throughout. Hence, for AlN, the resulting stress-thickness vs thickness curves were straight lines with a fixed slope (i.e. $_{\text{ins}}$ and $\overline{\sigma_i}$ were the same) having an average mean-stress of (1.5 ± 0.1) GPa across all wafers. Large tensile stress in AlN is known to be a pre-requisite for improved quality of the subsequent layers [51] and its reproducibility allows a comparison of the characteristics of different buffers on the same starting platform with confidence.

4.3. AlGaN buffers with 1.0 μm thickness

For the AlGaN layers, the changes of slope between consecutive layers are noticeable. Additionally, in contrast to the NL, the slope during the growth of the individual layers is not constant but changes as the layer grows thicker. From these stress-thickness versus thickness plots, the extracted values of instantaneous stresses at the beginning and the end of each layer are annotated in figure 3. Qualitatively, it can be seen that (a) the $_{\text{ins}}$ values at each interface change abruptly, and (b) all the layers start with a high compressive stress that reduces as the thickness increases (hence the slope becomes shallower). The only exception to the latter was the $Al_{0.83}Ga_{0.17}N$ layer in both sample A13 and sample B13. Almost zero instantaneous stress throughout for this layer indicates complete relaxation from the beginning. However, the samples C13 and D15 with a composition of $x \sim 0.78$ in the first AlGaN layer and grown on an identical AlN template as the sample B13, immediately starts to grow with compressive $_{\text{ins}}$ of ~ -0.5 GPa. This can be explained considering that relaxed $Al_{0.83}Ga_{0.17}N$ and $Al_{0.78}Ga_{0.22}N$ possess $\sim 0.41\%$ and $\sim 0.54\%$ lattice mismatch with relaxed AlN. Thus, a maximum of ~ -2.1 GPa and ~ -2.7 GPa compressive stress, respectively, would be available for their pseudomorphic growth on relaxed AlN. However, for AlN grown with a tensile stress of $+1.5$ GPa, the lattice mismatch reduces to $\sim 0.12\%$ and $\sim 0.25\%$, respectively and hence, the effective source of compressive stress becomes much lower than the theoretical maximum. We note that Yamaoka *et al* [32] had also observed negligible change in the curvature during the growth of the $Al_{0.75}Ga_{0.25}N$ layer of their 3-step AlGaN buffer. However, the low signal-to-noise

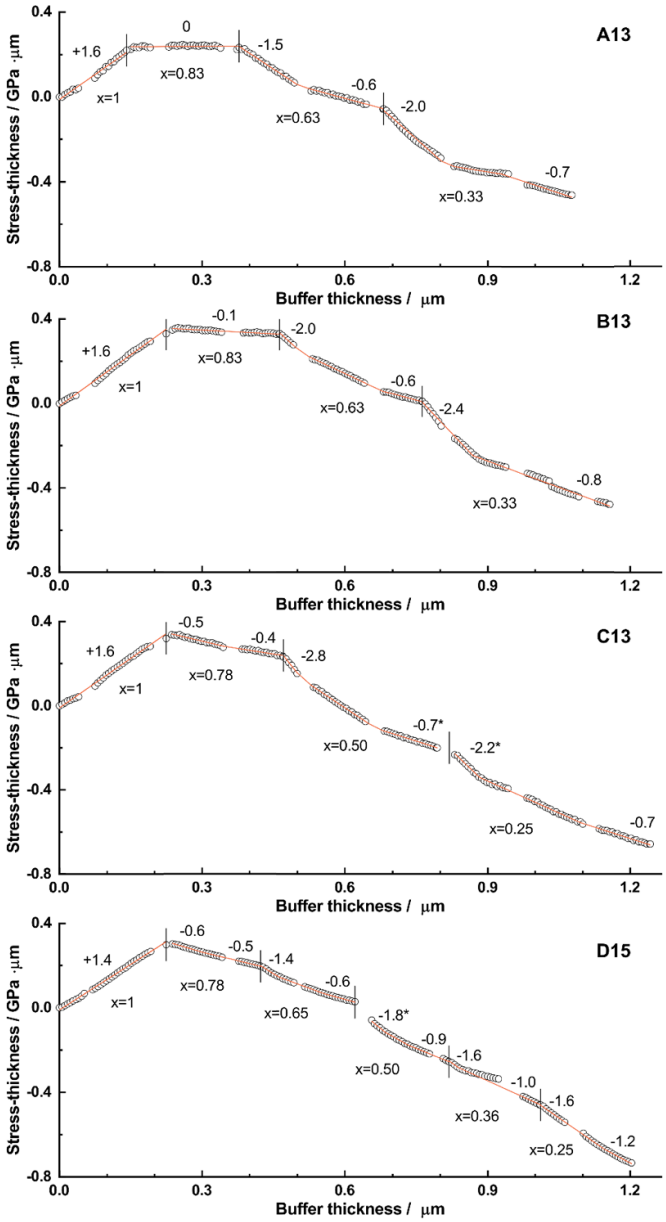

Figure 3. Evolution of real-time stress-thickness during the growth of the NL and AlGaN layers for the structures with 1 μm buffers. The vertical lines delineate different AlGaN layers and their specific AlN mole-fractions (x) are annotated. Open symbols represent experimental data, and the orange solid lines represent segmented line-fits to the experimental data. The extracted values of instantaneous stress at the beginning and end of each layer are marked. In case of overlap of a discontinuity in the data (arising from the extinction of the laser signal) with the beginning (or end) of a layer, the instantaneous slope right after (or before) such features is calculated instead and marked with an asterisk ('*'). Similar to figure 2, the number of shown experimental data points has been reduced for visual clarity.

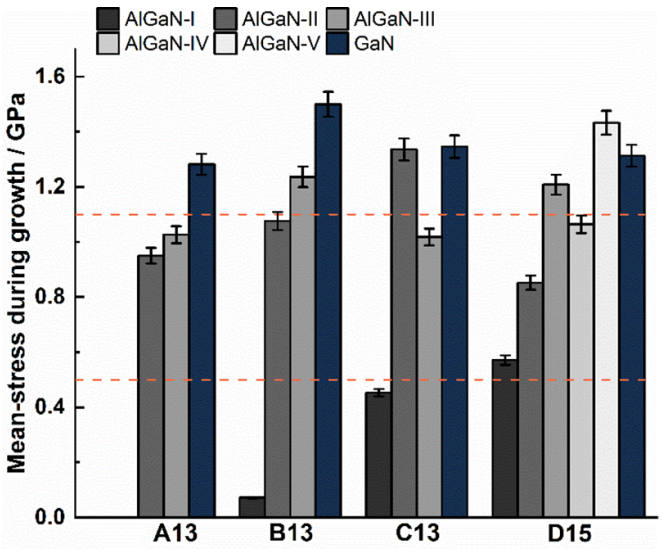

Figure 4. The magnitudes of the compressive mean-stress of the individual AlGaN and GaN layers for the four structures with 1 μm AlGaN buffers. Note that the values are not normalized for their thickness and the error bars are standard deviations that arise from the thickness variation (a maximum of 3%) across the 6-inch wafer. The lower and upper horizontal lines represent the estimated tensile thermal stress for AlN and GaN, respectively, for expansion co-efficient difference with silicon due to cooldown from growth temperatures, taken from ref. 8. The values for individual AlGaN layers are expected to lie in between.

ratio of their *in situ* data during their AlN growth precludes us from commenting on the associated stresses, though a similar mechanism is likely to be involved. In a similar vein, continuously graded AlGaN buffers have also shown this characteristic where induction of compressive stress does not start before the composition becomes lower than a certain AlN mole fraction [4, 52]. It is reasonable to expect that in addition to the final stress-state of the AlN layer, the rate of stress relaxation in the AlGaN layer itself will determine the exact composition for transition to compressive stress.

In addition, two other features are also apparent from the data in figure 3. First, a comparison between sample B13 and sample A13 shows that even a mere 100 nm increase in AlN NL thickness results in a significantly higher initial $_{ins}$ for most layers on top (e.g. −2.0 GPa compared to −1.5 GPa for $Al_{0.63}Ga_{0.37}N$, and −2.4 GPa compared to −2.0 GPa for $Al_{0.33}Ga_{0.67}N$). Second, both sample D15 and sample C13 had identical starting and end compositions of the buffer, however, the initial $_{ins}$ at the beginning of each of the AlGaN/AlGaN interfaces of the 5-step buffer of sample D15 are found to be smaller compared to the 3-step buffer of sample C13. The GaN layers grown under identical conditions on top of all these buffers were compressive throughout their growth (see figures S5 and S7 in the supplementary material) albeit the cumulative magnitude of the stresses was buffer-specific as discussed below. In figure 4, the magnitudes of compressive mean-stress ($\overline{\sigma_i}$) at the growth temperature for each AlGaN and GaN layer of the heterostructures discussed so far are plotted. Note that the calculated mean-stress of the $Al_{0.83}Ga_{0.17}N$ layer of A13 was very small and tensile ($\overline{\sigma_i}$ = +0.03). Considering the error bars, it is not included in this plot. A direct comparison between the samples A13 and B13, which differ only in the thickness of the AlN NL, clearly shows that each AlGaN layer of the latter induced more compressive stress. Understandably, the integrated mean stress ($\overline{\sigma_i}$) of each layer is dictated by the starting value of $_{ins}$ together with its rate of decay with thickness. As the thickness increases the initial stress decays further, which effectively lowers the integrated $\overline{\sigma_i}$ for a thicker layer even if the starting $_{ins}$ and relaxation rate are the same. Hence, given the identical thicknesses of the AlGaN layers in both samples (A13 and B13), the higher $\overline{\sigma_i}$ can be attributed to the higher starting stresses for the latter as observed in figure 3. Notably, at room temperature, a layer will have contributed with a net compressive stress only if $\overline{\sigma_i}$ at growth temperature is compressive and larger in magnitude than the tensile thermal stress that will be generated by cooling down from growth temperature (for comparison the thermal stress magnitudes for AlN and GaN are represented as horizontal dashed lines in the figure). Hence, it can be readily identified that the first AlGaN layer of each structure ($\overline{\sigma_i}$ from +0.03 GPa for A13 to −0.57 GPa for D15) falls short to fulfil this criterion. Also, as a general trend, the further a layer is away from the AlN NL, it is seen to have a higher $\overline{\sigma_i}$ even if the layer has a larger thickness. Hence it is important to notice, that in all the structures in figure 4, the GaN layer which is two to five times thicker than the individual AlGaN buffer layers, in general grows with the most amount of compressive stress with $\overline{\sigma_i}$ being −1.28 GPa, −1.50 GPa, −1.35 GPa, and −1.31 GPa for A13, B13, C13, and D15, respectively. As discussed later, this mean-stress at growth temperature can be an important indicator to compare the 'effective' contribution of the same layer in different structures, and the reason behind the different outcomes can be investigated and optimized. It thus becomes evident that even in similarly thick step-graded AlGaN buffers, the design of the layers can tune the degree of compression in the GaN layer grown on top. In devices, this GaN layer would be the nitride layer involved in carrier transport, injection, and recombination depending upon the functionality. Therefore, it is necessary to scrutinize whether apart from strain, the morphological and structural properties of GaN are affected as well. However, though Nomarski microscopy images and AFM scans did not reveal any difference in topography, a systematic difference was indeed observed in the structural qualities through HRXRD analysis. This is evident from figure 5, which shows that the post-growth ω-FWHM values of the skew-symmetric $20\bar{2}1$ XRD reflection is anticorrelated with the real-time mean-stress of the GaN epi-layer i.e. structures generating larger compressive stress have smaller FWHMs. More specifically, the GaN in samples B13 and A13 had the lowest and the highest FWHM of 639 arc-sec and 780 arc-sec, respectively, whereas the samples C13 and D15 had intermediate values of 692 arc-sec and 706 arc-sec. Notably, for epilayers with high dislocation density ($>5 \times 10^8$ cm^{-2}), broadening of off-axis $20\bar{2}1$ rocking curves is dominated by the in-plane twist related to local lattice distortions caused by TDs with edge-component (i.e. pure-edge and mixed type dislocations) [53]. In the literature, for estimation of edge dislocation

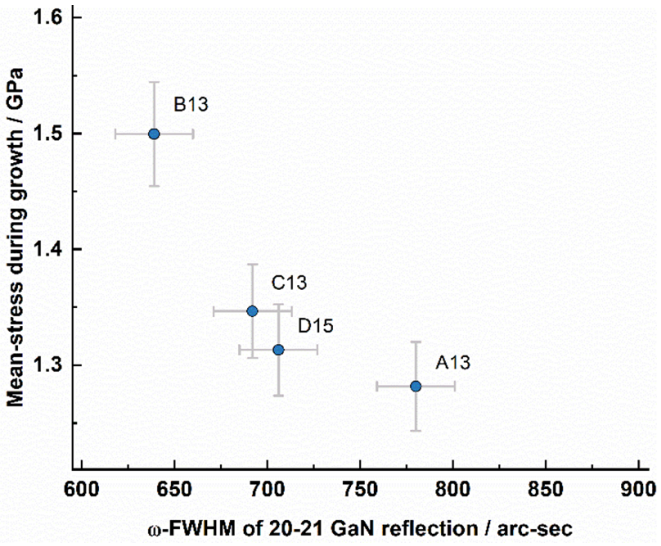

Figure 5. The magnitude of the mean compressive stress for the identically grown GaN layers on each buffer show a clear relationship with the HRXRD 20–21 peak broadening of the same. The horizontal error bars of the reflection peaks denote the measurement resolution dictated by the breadth of the direct beam.

density from the ω-FWHM (β) of this reflection (which has a high 75° inclination angle χ between reflection plane and c-plane surface), models have been developed considering either a random dislocation distribution or a mosaic structure that has dislocations only at grain boundaries. For GaN-on-Si epilayers with intrinsically high dislocation densities, studies have confirmed that the random distribution is the more appropriate approximation [54]. As per this model, the ω-FWHM is related with the density of randomly distributed dislocations with edge-component by

$$D_e = \frac{\beta^2}{4.35 b_e^2} \tag{5}$$

where $\overline{b_e}$ is the associated burgers vector length. This formula predicts 2.2 $\times$ 10^9 cm^{-2}–3.2 $\times 10^9$ cm^{-2} dislocations with edge-component (i.e. pure-edge and mixed) in the top GaN layer for the four structures in this series with their densities decreasing with increasing mean-stress. These values are well within the ranges of cross-sectional transmission electron microscopy (TEM) observed [4–7, 55] dislocation densities for GaN-on-Si. It is worth mentioning that the exact numbers may still differ from the latter if some of these dislocations are localized in arrays or at grain boundaries [54]. Nonetheless, the trend among the structures studied in this work is indeed expected to be meaningful. Apart from the $20\bar{2}1$ XRD reflection, the ω-FWHM of the 0002 reflections were also analyzed which can provide a measure of lattice-tilts and relates to the density of dislocations with screw-character (i.e. pure-screw and mixed type dislocations). However, within the small spread of observed values (596 arc-sec to 642 arc-sec) no obvious relation could be established with the mean stress of the GaN layer (see figure S6 in the supplementary material). This suggests that pure-screw and mixed dislocations do not vary

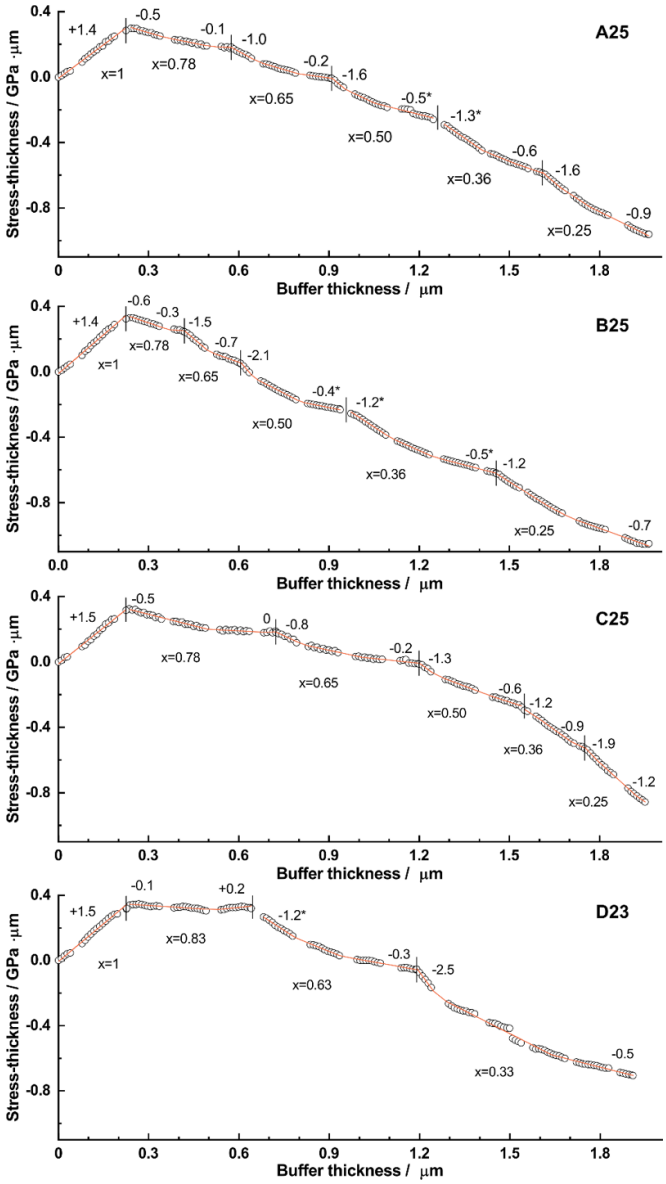

Figure 6. Evolution of real-time stress-thickness during the growth of the NL and AlGaN layers for the structures with 1.7 μm buffers. Open circles are experimental data points, and the solid curves are line segments fitted to the data. All the notions of figure 1 are similarly applicable. Note the difference among the stress-thickness values at the end of the final AlGaN layer which indicates different amount of accumulated compressive stress by the buffer itself. In these images, one representative experimental data point is shown for approximately every 5 nm.

appreciably among the structures and implies that GaN layers with a lower density of edge-type dislocations grow with higher mean stresses.

4.4. AlGaN buffers with 1.7 μm thickness

Next, the same sequence of characterizations was applied to analyze the structures with 1.7 μm buffers that had different thickness ratios among the AlGaN layers. The stress-thickness versus thickness plots for this series are displayed in figure 6. Similar to the structures with 1 μm buffers, the real-time decay

of the initial compressive stress of the AlGaN layers is prominent. Moreover, for layers grown on the same underlying buffer, a direct comparison can be made on the reduction of stress with increasing thickness. For instance, for the 5-step buffer of the samples B25, A25, and C25 initial −0.5 GPa−−0.6 GPa stress for the $Al_{0.78}Ga_{0.22}N$ layer relaxes to −0.3 GPa, −0.1 GPa, and finally to 0.0 GPa in the upper part of the layer as the layer is grown to 200 nm, 350 nm, and 500 nm thickness, respectively. Correlated with the decreasing final stress of this very first AlGaN layer, the initial $_{ins}$ of the following $Al_{0.65}Ga_{0.35}N$ layer becomes −1.5 GPa, −1.0 GPa, and −0.8 GPa for B25, A25, and C25, respectively. This proportionate 'transfer' of instantaneous stress between successive layers can also be observed for other layers of these 5-step buffers. In addition, it is observed that the $Al_{0.83}Ga_{0.17}N$ layer of D23 started with a meager compressive stress of −0.1 GPa but had a final $_{ins}$ of +0.2 GPa after growing to 420 nm thickness. This is evidence that a layer not only relaxes the initial compressive stress, but eventually can transition to the tensile regime during the growth itself.

The mean-stresses for these 1.7 μm buffers and the corresponding GaN layers are shown in figure 7. Clearly, even with equal thickness and nearly equal difference in AlN mole fraction (11% to 15%), each successive AlGaN layer of the sample A25 acquires more mean-stress than the previous layer. This can be attributed to the progressively increasing initial and/or final instantaneous compressive stress in each successive layer (refer to the stress-thickness data of figure 6). Moreover, a comparison of this structure with the other two 5-step 1.7 μm buffers reveals the influence of thickness ratio on stress accumulation. The first two AlGaN layers of sample B25 and the last two buffer layers of sample C25 likely benefit from their lower thicknesses and accumulates more compressive $\overline{\sigma_i}$ than the layers with same composition in the structure A25. By a similar argument, for these two asymmetric buffers, layers which were grown thicker than their A25 counterpart have less compressive stress on average. Notably, the reproducibility of these observations has been confirmed by repeating the growth of the AlGaN/AlN buffers (i.e. without the GaN layer) on separate growth runs. Also, in this series in figure 7, the sample D23 had the same total thickness but only three AlGaN layers. Hence, compared to the 5-step buffers, the individual AlGaN layer thicknesses of D23 had to be increased to achieve the total buffer thickness. This effectively resulted in a smaller mean-stress from the viewpoint of the individual layers as well as the complete AlGaN buffer stack. Yet, on this 'relaxed' buffer, the mean compressive stress of the 1 μm thick GaN on top was quite large at −1.63 GPa. In-fact, considering the error margins, this is equivalent to the −1.67 GPa mean-stress for the GaN layer of the sample C25 which was the highest noted in this investigation. It is worth mentioning that similar to the 1 μm thick structures in the previous section where the symmetric buffer of the sample D15 resulted in the least compressive GaN of that series, for this thicker series also the compressive stress was the lowest for the GaN layer on top of the symmetric 5-step buffer (as in A25) with a mean stress of just $\overline{\sigma_i} = -1.33$ GPa.

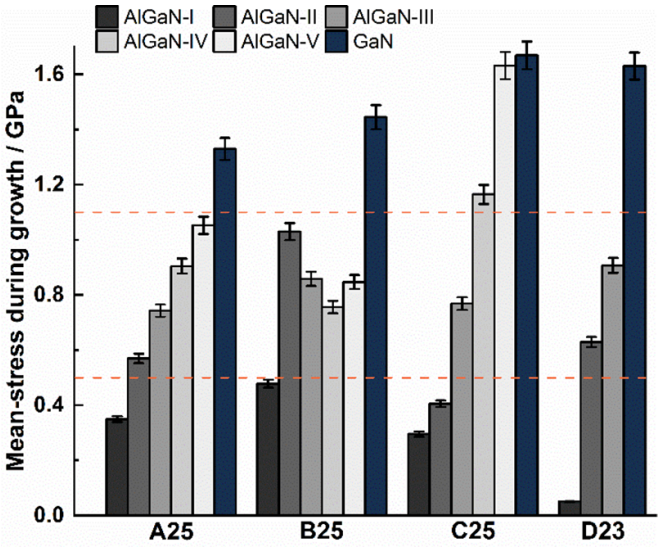

Figure 7. The magnitudes of the compressive mean-stress of the AlGaN and GaN layers for the four 1.7 μm buffers. Similar to figure 4, the estimated thermal stresses (tensile) for AlN and GaN due to cooldown are marked as the lower and the upper horizontal lines.

As with the 1 μm buffers, Nomarski images and AFM scans do not reveal any noticeable variation in surface topography (see figures S1 and S2 in the supplementary material) for this series, but the mean-stress of the GaN layer indeed show a similar dependence on the XRD ω-FWHM of the $20\bar{2}1$ reflection peaks. As plotted in figure 8, the structures with the highest mean-stresses for GaN, C25 and D23 also have the lowest broadening among all the investigated buffers with values of 621 arc-sec and 623 arc-sec, respectively. In contrast, the GaN layer of the sample A25 that has the least compressive mean-stress possesses a large FWHM of 893 arc-sec. From the same relationship between ω-FWHM of $20\bar{2}1$ reflection and dislocations with edge-character discussed in section C, densities from 2.0×10^9 cm^{-2} to 4.2×10^9 cm^{-2} are estimated for the GaN layers in this series.

It is important to note that this influence of the underlying buffer layers persisted for GaN layers thicker than 1 μm. For a separate study, we have grown uncracked thicker GaN layers on AlGaN buffer designs as of samples B25 and D23. Whereas the ω-FWHM of $20\bar{2}1$ reflection was 695 arc-sec for 1.0 μm GaN on the buffer of B25, it reduced to 577 arc-sec and 471 arc-sec for 2.0 μm and 3.0 μm thick GaN layers on the same buffer, respectively. In comparison, a 2.5 μm GaN layer grown under the same conditions on the buffer of sample D23 had an ω-FWHM value of 419 arc-sec. It is important to note that in addition to TDs, interfacial misfit dislocations further broaden ω-FWHMs and this contribution is higher for thinner layers. Still, the smaller ω-FWHM of the 2.5 μm GaN on buffer of D23 compared to the 3.0 μm thick GaN on the buffer of B25 confirms the superiority of the former. This also emphasizes the merit of buffer optimization in contrast to efforts to improve the defect-density by growing larger and larger thicknesses of the functional layers.

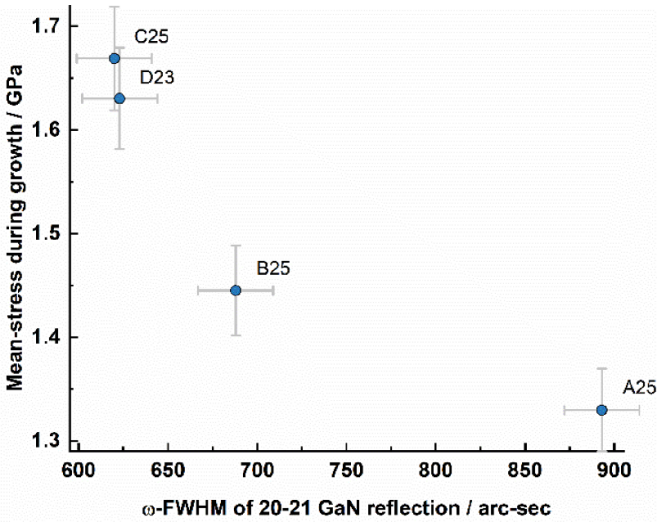

Figure 8. The GaN layer on the 1.7 μm thick buffers also exhibited the relationship among the mean compressive stress during layer growth and the broadening of the reflection, similar to the GaN layers on 1 μm thick step-graded buffers.

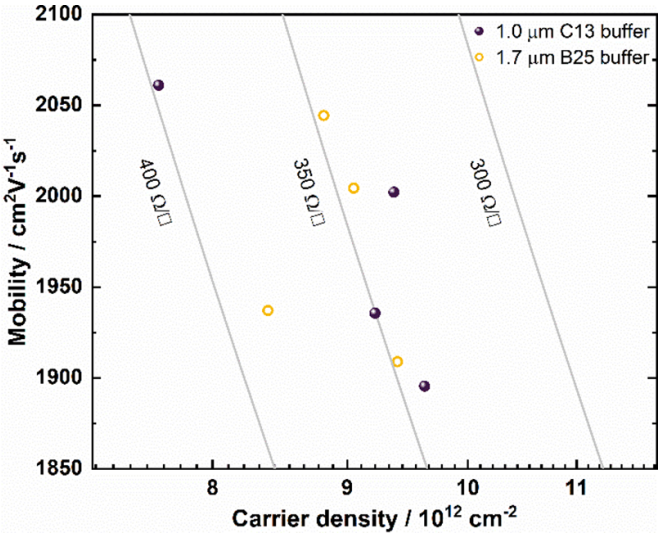

Figure 9. Measured room-temperature sheet-carrier densities and Hall mobilities for samples from the AlGaN/GaN HEMT structure with the 1 μm buffer of C13 (symbol: spheres) and the 1.7 μm buffer of B25 (symbol: open circles). The solid lines represent iso-contours of sheet-resistances from 300 $\Omega\,\square^{-1}$ to 400 $\Omega\,\square^{-1}$ with different carrier densities and mobilities. Given the van der Pauw sample geometry, the upper bound of uncertainty in the calculated Hall-mobilities are expected to be less than 10%.

4.5. Carrier statistics of high electron mobility transistor (HEMT) heterostructures with AlGaN barrier

Finally, carrier transport measurements were performed on additional HEMT heterostructures. These had a ∼19 nm $Al_{0.2}Ga_{0.8}N$ barrier and a ∼1 nm AlN exclusion layer grown on top of the GaN templates in the same run. Previously, Yamaoka *et al* have reported an increase in mobility (and decrease in sheet-resistance) with increase in buffer thickness up to 4 μm for GaN-on-Si heterostructures which the authors have credited to improved crystal quality [32]. In our study, to probe GaN layers with similar microstructure (i.e. presumably with comparable density of defects such as dislocations, which are well known scattering centers) but different buffer thicknesses underneath, the 1.0 μm buffer of C13 and the 1.7 μm buffer of B25 were selected for this experiment based on the nearly identical $20\bar{2}1$ ω-FWHM values of GaN grown on these buffers. For Hall-effect characterization, samples were prepared from four different locations of each HEMT wafer, and the evaluated room-temperature (RT) carrier densities and mobilities are plotted in figure 9. As shown, the measured carrier density for the samples varied from $\sim 0.8 \times 10^{13}$ cm^{-2} to 1.0×10^{13} cm^{-2}. These high-densities remained unchanged even at liquid N_2 temperatures (77 K) along with a negative Hall-coefficient throughout (not shown). This proved that the probed charge layers were indeed the two-dimensional electron gases (2DEG) formed at the barrier/channel interface. These high electron densities were accompanied by RT Hall mobilities that varied across the wafer from 1895 cm^2 V^{-1} S^{-1} to 2061 cm^2 V^{-1} S^{-1} for the 1.0 μm buffer and from 1909 cm^2 V^{-1} S^{-1} to 2044 cm^2 V^{-1} S^{-1} for the 1.7 μm buffer. Even for wafers with low-bow, such small scatter of values across the large-area wafers are expected [29, 56]. It is worth mentioning that studies have shown that the strain state of the GaN layer can induce a relaxation of the AlGaN barrier and in turn adversely affect the 2DEG [57, 58]. However, the equally good transport properties and low RT sheet-resistances $(\sim 350\ \Omega\ \square)^{-1}$ of the studied HEMT structures neither indicate the presence of such an effect for this barrier composition nor show any tangible influence of the buffer thickness for the structurally optimized GaN layer on top.

5. Discussion

To maximize device yield for GaN-on-Si, in addition to crack prevention, the wafer bow must be small to satisfy the processing compliance ($<\pm 50$ μm). This can be ensured by keeping the net mean-stress (i.e. after contribution of residual stresses from all the layers) at room-temperature sufficiently low. It is evident that the compressive stress during growth is the only 'handle' that can be engineered to achieve the above objectives as optimum growth temperatures (∼1000 °C) which cause the post-growth tensile stress due to the thermal expansion differences, are typically fixed. For any two consecutive AlGaN layers, the difference in composition (set by design) as well as the final stress-state of the lower layer fixes the maximum possible starting-stress in the upper layer. However, the decay mechanism of this initial value certainly warrants further consideration. Previous experimental studies [59–65] have established that in coalesced wurtzite III-nitride layers, relaxation of compressive strain is predominantly governed by inclination of edge-dislocations away from the [0001] direction which effectively projects a

misfit-segment on the basal plane (e.g. by bending a pure a-type TD with $\bar{b}_e = \pm\frac{1}{3}\left[11\bar{2}0\right]$ towards the $\pm\left[1\bar{1}00\right]$ directions). The activation energy for the involved climb kinetics has been formulated [66, 67] to be directly proportional to the magnitude of compressive stress of the incremental layer (i.e. to the instantaneous stress). Thus effectively, larger compressive stresses strive to bend the dislocations more [59, 64]. As larger inclination angles have a larger misfit projection and hence lead to greater relaxation, this mechanism may seem contrary to the objective of growing the layers in a compressive growth regime. However, such a bending process greatly facilitates edge dislocations with opposite burgers vectors to come closer, react, and potentially annihilate each other. This creates a unique opportunity to utilize (and partially consume) the compressive stress of the buffer itself for reduction of the density of dislocations generated in the NL. As lattice-mismatch stresses are typically larger than the thermal stress, it thus seems plausible to trade-off some compressive stress without compromising the ability to yield flat wafers.

The theoretical models [60–64, 68] for dislocation inclination in III-nitrides predict that strain relaxation in a layer is directly proportional to the TD density. Understandably, between two structures grown on the same underlying AlGaN composition (with comparable final strain-state) GaN would retain more compressive stress in the one with fewer dislocations. This explains the observed trends between mean-stresses and $20\bar{2}1$ FWHMs for the GaN layers investigated. Also, it becomes apparent that different AlGaN buffer designs (thickness and composition steps) have different efficiency in blocking the propagation of TDs as the identical growth condition and thickness of the GaN layers cannot be held responsible for their variation in the defect structure. The decay of instantaneous stress (i.e. relaxation) as indicated by the changing slope of the stress-thickness versus thickness curves for all the layers in the buffers provide evidence that bending of dislocations occurs during growth. In terms of the mechanism, TEM investigations [7, 64] have previously shown that abrupt compositional changes in AlGaN layers induce immediate change in the dislocation line direction. In view of those experimental findings, the interfaces between the studied AlGaN buffer layers with different compositions (and including the one between the final buffer layer and the GaN) are expected to force dislocation inclination and interaction. This is further supported by the fact that the recorded stresses were the highest at the beginning of each layer which would facilitate such kinetics as per the theoretical models stated earlier. It is worth noting that the magnitudes of the observed starting stresses were always smaller than theoretically anticipated for pseudomorphic growth (for the different compositions studied, the predicted values of starting stresses at growth temperature range from -4.9 GPa to -1.7 GPa for respective interfaces considering a fully relaxed underlayer and would be even larger for a strained underlayer by the magnitude of compressive stress in the same). Thus, some relaxation at a few nm thicknesses due to the introduction of misfit dislocations [69] is probable as well. However, this is outside the detection limit of the curvature measurement system used in this study. It is worth mentioning that some contributions from other mechanisms including dislocation glide and/or lateral motion could also be involved, and a separate cross-sectional TEM study of buffer layers is planned in future to investigate this.

Given the role of composition changes in these buffers, the effect of the number of steps warrants a discussion. When the initial and final compositions are fixed, increasing the number of steps results in thinner individual AlGaN layers for the same total thickness. This may seem beneficial as it restricts the layers from undergoing large relaxation. However, an increased number of steps also reduces the compositional differences between successive layers and in-turn the available starting stresses. Owing to these competing factors, it can be observed that dividing the same end-compositions into 5-steps (as in sample D15) compared to 3-steps (as in the structure C13) does not provide any additional improvement in terms of mean-stress or XRD FWHM for the final GaN layer. Furthermore, when the same 5-step buffer was proportionately increased to achieve a cumulative thickness of 1.7 μm for sample A25, the individual layers which now became thicker, suffered more relaxation in addition to the already low initial stresses. Thus, a comparison of the rocking curve and mean-stress data of their GaN layer indicates that any advantage which may have been provided by the added thickness to enhance opportunity for dislocation interaction, was negated. Interestingly, even for 5-step buffers, tuning the thickness ratios can overcome the shortcomings of the symmetric design. For example, keeping the total thickness the same, whilst thinning the first two AlGaN layers ensured their higher mean-stresses and in-turn larger initial compressive stresses at the associated two interfaces for the buffer of sample B25. On the other hand, making the final two AlGaN layers thinner had produced a similar effect for the corresponding layers and interfaces of the C25 heterostructure. As a result, in terms of both defect-structure and cumulative compressive stress, the GaN layer on either of these buffers was superior to that of sample A25. Moreover, between these two asymmetric buffers, it was observed that a higher proportion of AlGaN layers with high Al content resulted in a GaN layer on top with even better microstructure. Note that this design is directly opposite to the usual structure consisting thinner high Al composition layers and thicker low Al composition layers which have been typically followed to date (as evidenced by the references in this article). It is plausible that the structure with thicker high Al composition layers forces more dislocations to interact early in the buffer when their density is high, increasing the probability of dislocations with opposite burgers vector reacting and annihilating each other. Although we have not found other instances of this asymmetric design for step-graded buffers in the literature, interestingly Yang *et al* [70] have shown that among several continuously AlGaN graded buffers, those with thicker high Al-composition regions and thinner low Al-composition regions showed a lower ω-FWHM of the $10\bar{1}2$ XRD reflection and larger compressive stress in Raman measurement, agreeing well with our data. Nonetheless, further investigation is needed to confirm whether this is applicable to compositions other than those implemented in this article.

Based on these collective findings, it can be established that the buffer thickness is not an independent criterion for epilayer optimization and unreasonably thick buffers are not required to achieve device quality GaN layers. Along with reduced material consumption, thinner buffers may also improve heat extraction from devices with a reduction in the thickness of the $Al_xGa_{1-x}N$ alloys which have an order less thermal conductivity [71, 72] (for $90 > x > 10$) compared to their binary constituents. As our work shows, it now becomes evident why even a single and thin AlGaN buffer [27–29] can realize crack-free GaN heterostructures by providing enough compositional difference at the two interfaces. Still, at times, a certain buffer thickness needs to be achieved from operational perspective (such as to sustain a certain breakdown voltage). From a structural perspective, for step-graded buffers, it is suggested to distribute the intended total buffer thickness in minimum number of steps with sharp difference in compositions and only increase the number of steps in-case the integrated mean-stress of the layer becomes so low that the wafer bow is out of compliance.

Though the different buffers may act to reduce the dislocation densities with different efficiencies, it is understandable that any reduction in their numbers at the source itself (i.e. in the AlN layer which usually have a dislocation density $>10^{10}$ cm^{-2}) would amplify the efficiency of the same buffer. Notably, in the NL layer, the dislocation density is extremely high and an increase in thickness may aid in their random interaction even in the tensile regime. In this investigation, HRXRD characterization of a sample consisting of only a 150 nm thick AlN NL showed ω-FWHM values of 1170 arc-secs and 2730 arc-secs for the 0002 and $20\bar{2}1$ XRD reflection of AlN, respectively. For a 250 nm thick NL, these values reduced to 895 arc-sec and 2268 arc-sec. As mentioned previously, HRXRD of the thicker AlN layer would have a smaller contribution from the defects at the AlN/Si interface. Nonetheless, such large reductions in ω-FWHM indeed indicate a reduction in dislocation density with increased thickness of the AlN NL. This is believed to be the cause behind the difference in performance between the samples A13 and B13. There is a caveat: a large increase in thickness of the AlN will proportionately increase the contribution of tensile stress along with possibilities of cracking the AlN during growth. Instead, though not attempted in this study, improving the structural quality of the NL through optimization of growth conditions should offer a better route to increase the buffer efficiency further. In addition, changing the growth parameters of the GaN layer may also alter the rate of relaxation of the starting compressive stress by influencing the growth kinetics and dislocation bending. For instance, GaN grown by molecular beam epitaxy (MBE) on silicon experiences a smaller tensile thermal stress owing to the lower growth temperatures compared to MOCVD and does not require the growth of an AlGaN buffer. Nonetheless, a dependence between crystal quality and relaxation rate of the lattice-mismatch stress originating from the underlying AlN has been observed [73] which suggests that the mechanisms involved may be universal. In such structures, modifying the growth temperature, nitrogen source, and V/III molar ratio have proven to be useful for strain engineering [73–75]. Analogous MOCVD growth parameters could aid in tuning the stresses in the GaN layer provided that the electrical or optical properties are not adversely affected.

6. Conclusion

In conclusion, *in situ* wafer curvature measurements during MOCVD deposition and post-growth HRXRD measurements have provided valuable insight for non-destructive analysis and design of step-graded AlGaN buffers on silicon substrates. As the initial lattice-mismatch stresses generated at the AlN/AlGaN, AlGaN/AlGaN, and AlGaN/GaN heterointerfaces were found to control the accumulated mean-stresses in the buffers and GaN layers, the compositions (and effectively their compositional differences) of the individual AlGaN layers are suggested to be the most crucial parameter in buffer design. In addition, for the probe GaN layers, an anti-correlation was observed between the mean-stress of the layer and broadening of the HRXRD peaks sensitive to the edge-type dislocation density. This shows that the well-known dislocation inclination mechanism that relaxes compressive stress can be strategically used to force their annihilation and improve the microstructural quality while still preserving the amount of compressive stress required for crack evasion and bow control. It was also confirmed that for step-graded buffers, neither a proportional increase of the buffer thickness nor the number of steps guarantees a tangible improvement of the functional layers. However, our results also suggest that if changing the total thickness, the number of steps, or the individual compositions is not wanted, tuning the thickness ratio to increase the proportion of high Al content AlGaN layers may lead to better functional layers.

Data availability statement

The data that support the findings of this study are openly available at the following URL/DOI: https://doi.org/10.17863/CAM.91676.

Acknowledgments

This research was supported by the Engineering and Physical Sciences Research Council (EPSRC) under the grant ‘Hetero-print’: A holistic approach to transfer-printing for heterogeneous integration in manufacturing (EP/R03480X/1). Alexander M Hinz acknowledges the Deutsche Forschungsgemeinschaft for his Research Fellowship at the University of Cambridge. David J Wallis acknowledges the support of the EPSRC fellowship (EP/N01202X/2). The authors are grateful to Dr Menno J Kappers and Dr Gunnar Kusch for their critical suggestions. Saptarsi Ghosh thanks Kalyan Kasarla and Terry Devlin from Veeco™ for their support with the MOCVD reactor.

Conflict of interest

The authors have no conflicts to disclose.

ORCID iDs

Saptarsi Ghosh https://orcid.org/0000-0003-1685-6228
Alexander M Hinz https://orcid.org/0000-0002-8845-0086
Rachel A Oliver https://orcid.org/0000-0003-0029-3993

References

[1] Zhu D *et al* 2009 GaN-based LEDs grown on 6-inch diameter Si (111) substrates by MOVPE *Proc. SPIE* **7231** 723118
[2] Zhu D, Wallis D J and Humphreys C J 2013 Prospects of III-nitride optoelectronics grown on Si *Rep. Prog. Phys.* **76** 106501
[3] Chen K J, Haberlen O, Lidow A, Tsai C L, Ueda T, Uemoto Y and Wu Y 2017 GaN-on-Si power technology: devices and applications *IEEE Trans. Electron Devices* **64** 779–95
[4] Mohan N, Manikant; Soman R and Raghavan S 2015 Integrating AlGaN/GaN high electron mobility transistor with Si: a comparative study of integration schemes *J. Appl. Phys.* **118** 135302
[5] Weng X, Acord J D, Jain A, Dickey E C and Redwing J M 2007 Evolution of threading dislocation density and stress in GaN films grown on (111) Si substrates by metalorganic chemical vapor deposition *J. Electron. Mater.* **36** 346–52
[6] Sugawara Y, Ishikawa Y, Watanabe A, Miyoshi M and Egawa T 2016 Characterization of dislocations in GaN layer grown on 4-Inch Si(111) with AlGaN/AlN strained layer superlattices *Jpn. J. Appl. Phys.* **55** 05FB08
[7] Haeberlen M, Zhu D, McAleese C, Kappers M J and Humphreys C J 2010 Dislocation Reduction in MOVPE grown GaN layers on (111)Si using SiNx and AlGaN layers *J. Phys.: Conf. Ser.* **209** 012017
[8] Raghavan S and Redwing J M 2005 Growth stresses and cracking in GaN films on (111) Si grown by metal-organic chemical-vapor deposition. I. AlN buffer layers *J. Appl. Phys.* **98** 023514
[9] Cheng K, Leys M, Degroote S, Van Daele B, Boeykens S, Derluyn J, Germain M, Van Tendeloo G, Engelen J and Borghs G 2006 Flat GaN epitaxial layers grown on Si(111) by metalorganic vapor phase epitaxy using step-graded AlGaN intermediate layers *J. Electron. Mater.* **35** 592–8
[10] Drechsel P and Riechert H 2011 Strain controlled growth of crack-free GaN with low defect density on silicon (111) substrate *J. Cryst. Growth* **315** 211–5
[11] Rafaja D, Fischer P, Barchuk M, Motylenko M, Röder C, Besendörfer S and Meissner E 2021 X-ray diffraction analysis and modeling of the depth profile of lattice strains in AlGaN stacks *Thin Solid Films* **732** 138777
[12] Lim S H, Bin Dolmanan S, Tong S W and Liu H 2021 Temperature dependent lattice expansions of epitaxial GaN-on-Si heterostructures characterized by in- and Ex-situ x-ray diffraction *J. Alloys Compd.* **868** 159181
[13] Ma J, Zhang Y, Li Y, Zhang T, Yao Y, Feng Q, Bi Z, Zhang J and Hao Y 2022 Mechanistic influence on uniformity of sheet resistance of AlGaN/GaN HEMT grown on Si substrate with the graded AlGaN buffer layers *Vacuum* **199** 110966
[14] Baca A G, Armstrong A M, Klein B A, Allerman A A, Douglas E A and Kaplar R J 2020 Al-rich AlGaN based transistors *J. Vac. Sci. Technol.* A **38** 020803
[15] Kneissl M, Seong T-Y, Han J and Amano H 2019 The emergence and prospects of deep-ultraviolet light-emitting diode technologies *Nat. Photon.* **13** 233–44
[16] Zhang H, Huang C, Song K, Yu H, Xing C, Wang D, Liu Z and Sun H 2021 Compositionally graded III-nitride alloys: building blocks for efficient ultraviolet optoelectronics and power electronics *Rep. Prog. Phys.* **84** 044401
[17] Spiridon B F *et al* 2021 Method for inferring the mechanical strain of GaN-on-Si epitaxial layers using optical profilometry and finite element analysis *Opt. Mater. Express* **11** 1643
[18] Wessling N K, Ghosh S, Guilhabert B, Kappers M, Hinz A M, Toon M, Oliver R A, Dawson M D and Strain M J 2022 Fabrication and transfer printing based integration of free-standing GaN membrane micro-lenses onto semiconductor chips *Opt. Mater. Express* **12** 4606
[19] Xu P-Q, Jiang Y, Ma Z-G, Deng Z, Lu T-P, Du C-H, Fang Y-T, Zuo P and Chen H 2013 The Influence of graded AlGaN buffer thickness for crack-free GaN on Si(111) substrates by using MOCVD *Chin. Phys. Lett.* **30** 028101
[20] Yu X, Ni J, Li Z, Zhou J and Kong C 2014 Reduction in leakage current in AlGaN/GaN HEMT with three Al-containing step-graded AlGaN buffer layers on silicon *Jpn. J. Appl. Phys.* **53** 051001
[21] Remesh N, Chandrasekar H, Venugopalrao A, Raghavan S, Rangarajan M and Nath D N 2021 Re-engineering transition layers in AlGaN/GaN HEMT on Si for high voltage applications *J. Appl. Phys.* **130** 075702
[22] Li Y, Wang W, Li X, Huang L, Lin Z, Zheng Y, Chen X and Li G 2019 Stress and dislocation control of GaN epitaxial films grown on Si substrates and their application in high-performance light-emitting diodes *J. Alloys Compd.* **771** 1000–8
[23] Leung B, Han J and Sun Q 2014 Strain relaxation and dislocation reduction in AlGaN step-graded buffer for crack-free GaN on Si (111) *Phys. Status Solidi* **11** 437–41
[24] Arslan E, Ozturk M K, Teke A, Ozcelik S and Ozbay E 2008 Buffer optimization for crack-free GaN epitaxial layers grown on Si(111) substrate by MOCVD *J. Phys. D: Appl. Phys.* **41** 155317
[25] Besendörfer S, Meissner E, Tajalli A, Meneghini M, Freitas J A, Derluyn J, Medjdoub F, Meneghesso G, Friedrich J and Erlbacher T 2020 Vertical breakdown of GaN on Si due to V-pits *J. Appl. Phys.* **127** 015701
[26] Huang C C, Chang S J, Chuang R W, Lin J C, Cheng Y C and Lin W J 2010 GaN grown on Si(111) with step-Graded AlGaN intermediate layers *Appl. Surf. Sci.* **256** 6367–70
[27] Ishikawa H, Zhao G-Y, Nakada N, Egawa T, Jimbo T and Umeno M 1999 GaN on Si substrate with AlGaN/AlN intermediate layer *Jpn. J. Appl. Phys.* **38** L492–4
[28] Cheng J, Yang X, Sang L, Guo L, Hu A, Xu F, Tang N, Wang X and Shen B 2015 High mobility AlGaN/GaN heterostructures grown on Si substrates using a large lattice-mismatch induced stress control technology *Appl. Phys. Lett.* **106** 142106
[29] Cheng J *et al* 2016 Growth of high quality and uniformity AlGaN/GaN heterostructures on Si substrates using a single AlGaN layer with low Al composition *Sci. Rep.* **6** 23020
[30] Lin Y, Yang M, Wang W, Lin Z, Gao J and Li G 2016 High-quality crack-free GaN epitaxial films grown on Si substrates by a two-step growth of AlN buffer layer *CrystEngComm* **18** 2446–54
[31] Tripathy S *et al* 2012 AlGaN/GaN two-dimensional-electron gas heterostructures on 200 Mm diameter Si(111) *Appl. Phys. Lett.* **101** 082110
[32] Yamaoka Y, Kakamu K, Ubukata A, Yano Y, Tabuchi T, Matsumoto K and Egawa T 2017 Influence of the Al content of the AlGaN buffer layer in AlGaN/GaN

high-electron-mobility transistor structures on a Si substrate *Phys. Status Solidi* **214** 1600618
[33] Lee H-P, Perozek J, Rosario L D and Bayram C 2016 Investigation of AlGaN/GaN high electron mobility transistor structures on 200-Mm silicon (111) substrates employing different buffer layer configurations *Sci. Rep.* **6** 37588
[34] Reiher A, Bläsing J, Dadgar A, Diez A and Krost A 2003 Efficient stress relief in GaN heteroepitaxy on Si(111) using low-temperature AlN interlayers *J. Cryst. Growth* **248** 563–7
[35] Lin P-J, Tien C-H, Wang T-Y, Chen C-L, Ou S-L, Chung B-C and Wuu D-S 2017 On the role of AlN insertion layer in stress control of GaN on 150-Mm Si (111) substrate *Crystals* **7** 134
[36] Su J, Armour E A, Krishnan B, Lee S M and Papasouliotis G D 2015 Stress engineering with AlN/GaN superlattices for epitaxial GaN on 200 Mm silicon substrates using a single wafer rotating disk MOCVD reactor *J. Mater. Res.* **30** 2846–58
[37] Dadgar A 2015 Sixteen years GaN on Si *Phys. Status Solidi* **252** 1063–8
[38] Watanabe A, Takeuchi T, Hirosawa K, Amano H, Hiramatsu K and Akasaki I 1993 The growth of single crystalline GaN on a Si substrate using AIN as an intermediate layer *J. Cryst. Growth* **128** 391–6
[39] Keck P H and Broder J 1953 The solubility of silicon and germanium in gallium and indium *Phys. Rev.* **90** 521–2
[40] Ishikawa H, Yamamoto K, Egawa T, Soga T, Jimbo T and Umeno M 1998 Thermal stability of GaN on (111) Si substrate *J. Cryst. Growth* **189–190** 178–82
[41] Kadir A, Srivastava S, Li Z, Lee K E K, Sasangka W A, Gradecak S, Chua S J and Fitzgerald E A 2018 Influence of substrate nitridation on the threading dislocation density of GaN grown on 200 Mm Si (111) substrate *Thin Solid Films* **663** 73–78
[42] Choi F S, Griffiths J T, Ren C, Lee K B, Zaidi Z H, Houston P A, Guiney I, Humphreys C J, Oliver R A and Wallis D J 2018 Vertical leakage mechanism in GaN on Si high electron mobility transistor buffer layers *J. Appl. Phys.* **124** 055702
[43] Floro J A, Chason E, Lee S R, Twesten R D, Hwang R Q and Freund L B 1997 Real-time stress evolution during Si1-XGex heteroepitaxy: dislocations, islanding, and segregation *J. Electron. Mater.* **26** 969–79
[44] Chason E and Guduru P R 2016 Tutorial: understanding residual stress in polycrystalline thin films through real-time measurements and physical models *J. Appl. Phys.* **119** 191101
[45] Abadias G, Chason E, Keckes J, Sebastiani M, Thompson G B, Barthel E, Doll G L, Murray C E, Stoessel C H and Martinu L 2018 Review article: stress in thin films and coatings: current status, challenges, and prospects *J. Vac. Sci. Technol.* A **36** 020801
[46] Hess P 1996 Laser diagnostics of mechanical and elastic properties of silicon and carbon films *Appl. Surf. Sci.* **106** 429–37
[47] Dolbow J and Gosz M 1996 Effect of out-of-plane properties of a polyimide film on the stress fields in microelectronic structures *Mech. Mater.* **23** 311–21
[48] Huang S and Zhang X 2006 Extension of the stoney formula for film–substrate systems with gradient stress for mems applications *J. Micromech. Microeng.* **16** 382–9
[49] Qiang J, Jiang B, Dong Y, Roth B and Jiang F 2021 Extension of the stoney formula for the incremental stress of thin films *Appl. Phys. Lett.* **118** 091604
[50] Ghosh S, Hinz A M,Frentrup M,Alam S,Wallis D J and Oliver R A 2023 Research data supporting [Design of step-graded AlGaN buffers for GaN-on-Si heterostructures grown by MOCVD] [Dataset] (https://doi.org/10.17863/CAM.91676)
[51] Chandrasekar H, Mohan N, Bardhan A, Bhat K N, Bhat N, Ravishankar N and Raghavan S 2013 An early *in-situ* stress signature of the AlN-Si pre-growth interface for successful integration of nitrides with (111) Si *Appl. Phys. Lett.* **103** 211902
[52] Raghavan S and Redwing J 2005 Growth stresses and cracking in GaN films on (111) Si grown by metalorganic chemical vapor deposition II. Graded AlGaN buffer layers *J. Appl. Phys.* **98** 023515
[53] Moram M A and Vickers M E 2009 X-ray diffraction of III-nitrides *Rep. Prog. Phys.* **72** 036502
[54] Chierchia R, Böttcher T, Heinke H, Einfeldt S, Figge S and Hommel D 2003 Microstructure of heteroepitaxial GaN revealed by x-ray diffraction *J. Appl. Phys.* **93** 8918–25
[55] Marchand H, Zhao L, Zhang N, Moran B, Coffie R, Mishra U K, Speck J S, DenBaars S P and Freitas J A 2001 Metalorganic chemical vapor deposition of GaN on Si(111): stress control and application to field-effect transistors *J. Appl. Phys.* **89** 7846–51
[56] Cheng K *et al* 2012 AlGaN/GaN/AlGaN double heterostructures grown on 200 Mm silicon (111) substrates with high electron mobility *Appl. Phys. Express* **5** 011002
[57] Jiménez A, Bougrioua Z, Tirado J M, Braña A F, Calleja E, Muñoz E and Moerman I 2003 Improved AlGaN/GaN high electron mobility transistor using AlN interlayers *Appl. Phys. Lett.* **82** 4827–9
[58] Bougrioua Z, Moerman I, Nistor L, Van Daele B, Monroy E, Palacios T, Calle F and Leroux M 2003 Engineering of an insulating buffer and use of AlN interlayers: two optimisations for AlGaN–GaN HEMT-like structures *Phys. Status Solidi* **195** 93–100
[59] Raghavan S, Weng X, Dickey E and Redwing J M 2006 Correlation of growth stress and structural evolution during metalorganic chemical vapor deposition of GaN on (111) Si *Appl. Phys. Lett.* **88** 041904
[60] Follstaedt D M, Lee S R, Provencio P P, Allerman A A, Floro J A and Crawford M H 2005 Relaxation of compressively-strained AlGaN by inclined threading dislocations *Appl. Phys. Lett.* **87** 121112
[61] Romanov A E, Beltz G E, Cantu P, Wu F, Keller S, DenBaars S P and Speck J S 2006 Cracking of III-nitride layers with strain gradients *Appl. Phys. Lett.* **89** 161922
[62] Wang J F, Yao D Z, Chen J, Zhu J J, Zhao D G, Jiang D S, Yang H and Liang J W 2006 Strain evolution in GaN layers grown on high-temperature AlN interlayers *Appl. Phys. Lett.* **89** 152105
[63] Acord J D, Manning I C, Weng X, Snyder D W and Redwing J M 2008 *In Situ* measurement of stress generation arising from dislocation inclination in $Al_xGa_{1-x}N$:Si thin films *Appl. Phys. Lett.* **93** 111910
[64] Follstaedt D M, Lee S R, Allerman A A and Floro J A 2009 Strain relaxation in AlGaN multilayer structures by inclined dislocations *J. Appl. Phys.* **105** 083507
[65] Weinrich J, Mogilatenko A, Brunner F, Koch C T and Weyers M 2019 Extra half-plane shortening of dislocations as an origin of tensile strain in Si-doped (Al)GaN *J. Appl. Phys.* **126** 085701
[66] Raghavan S, Manning I C, Weng X and Redwing J M 2012 Dislocation bending and tensile stress generation in GaN and AlGaN films *J. Cryst. Growth* **359** 35–42
[67] Raghavan S 2011 Kinetic approach to dislocation bending in low-mobility films *Phys. Rev.* B **83** 052102
[68] Romanov A E and Speck J S 2003 Stress relaxation in mismatched layers due to threading dislocation inclination *Appl. Phys. Lett.* **83** 2569–71

[69] Holec D, Zhang Y, Rao D V S, Kappers M J, McAleese C and Humphreys C J 2008 Equilibrium critical thickness for misfit dislocations in III-nitrides *J. Appl. Phys.* **104** 123514
[70] Yang Y *et al* 2013 Effect of compositionally graded AlGaN buffer layer grown by different functions of trimethylaluminum flow rates on the properties of GaN on Si (111) substrates *J. Cryst. Growth* **376** 23–27
[71] Liu W and Balandin A A 2005 Thermal conduction in AlxGa1−xN alloys and thin films *J. Appl. Phys.* **97** 073710
[72] Tran D Q, Blumenschein N, Mock A, Sukkaew P, Zhang H, Muth J F, Paskova T, Paskov P P and Darakchieva V 2020 Thermal conductivity of ultra-wide bandgap thin layers—high Al-content AlGaN and β-Ga_2O_3 *Phys. Condens. Matter* B **579** 411810
[73] Baron N, Cordier Y, Chenot S, Vennéguès P, Tottereau O, Leroux M, Semond F and Massies J 2009 The critical role of growth temperature on the structural and electrical properties of AlGaN/GaN high electron mobility transistor heterostructures grown on Si(111) *J. Appl. Phys.* **105** 033701
[74] Cordier Y, Baron N, Chenot S, Vennéguès P, Tottereau O, Leroux M, Semond F and Massies J 2009 Strain engineering in GaN layers grown on silicon by molecular beam epitaxy: the critical role of growth temperature *J. Cryst. Growth* **311** 2002–5
[75] Aidam R, Diwo E, Rollbühler N, Kirste L and Benkhelifa F 2012 Strain control of AlGaN/GaN high electron mobility transistor structures on silicon (111) by plasma assisted molecular beam epitaxy *J. Appl. Phys.* **111** 114516